mater.scichina.com link.springer.com

Published online 30 July 2021 | https://doi.org/10.1007/s40843-021-1730-1
Sci China Mater 2022, 65(1): 78–84

Superior cycling stability of $H_{0.642}V_2O_5{\cdot}0.143H_2O$ in rechargeable aqueous zinc batteries

Yuetao Wang, Chuanxi Chen, Hengyu Ren, Runzhi Qin, Haocong Yi, Shouxiang Ding, Yang Li, Lu Yao, Shunning Li, Qinghe Zhao* and Feng Pan*

ABSTRACT To increase the service life of rechargeable batteries, transition metal oxide hosts with high structural stability for the intercalation of carrier ions are important. Herein, we reconstruct the crystal structure of a commercial V_2O_5 by pre-intercalating H^+ and H_2O pillars using a facile hydrothermal reaction and obtain a bi-layer structured $H_{0.642}V_2O_5{\cdot}0.143H_2O$ (HVO) as an excellent host for aqueous Zn-ion batteries. Benefiting from the structural reconstruction, the irreversible "layer-to-amorphous" phase evolution during cycling is considerably less, resulting in ultra-high cycling stability of HVO with nearly no capacity fading even after 500 cycles at a current density of 0.5 A g^{-1}. Moreover, a synthetic proton and Zn^{2+} intercalation mechanism in the HVO host is demonstrated. This work provides both a facile synthesis method for the preparation of V-based compounds and a new viewpoint for achieving high-performance host materials.

Keywords: aqueous battery, vanadium oxide, phase conversion, structural stability

INTRODUCTION

Recently, rechargeable aqueous Zn-ion batteries (RAZBs) with mild acid electrolytes have attracted considerable interest as promising next-generation batteries because of their great potential for high capacity delivery with lower cost and better safety than Li-ion batteries [1,2]. However, their industrial application is limited by issues in the Zn anode (corrosion, dendrite, and side reactions) [3,4] and cathode materials (capacity fading and sluggish reaction kinetics) such as MnO_2 [5–7], V_2O_5 [8–10], and Prussian blue analogue [11,12]. To increase the cycle life of the Zn anode, researchers have recently developed certain optimization strategies such as tuning electrolytes with additives [13], applying "water in salt" electrolytes [14], organic/inorganic coating [15,16], and utilizing 3D current collectors [17,18]. Furthermore, the electrochemical performance of cathode materials has been improved using optimization methods such as metal substitution [19], coating with conductive layers [20,21], applying pre-intercalation strategy [22,23], and defect engineering [24,25]. Pre-intercalation engineering provides a basic and effective insight for optimizing the structure and correlated electrode performance of Mn- and V-based host materials.

For V-based host materials, Yao *et al.* [26] emphasized the important role of pre-intercalating ions/molecules for facilitating the electrode reactions in aqueous batteries, which display multiple advantages for enhancing intrinsic conductivity, activating reaction sites, promoting diffusion kinetics, and stabilizing structural integrity. To date, considerable efforts have been exerted to enhance the electrode performance of V_2O_5-based cathode by pre-intercalating alkaline ions (Li^+ [27], Na^+ [28], and K^+ [29]), alkaline earth metal ions (Mg^{2+} [30], Ca^{2+} [31], and Ba^{2+} [32]), conductive organic species (polyaniline [33], poly (3,4-ethylenedioxythiophene) [34]), and structural water [35,36]. However, the structure variations because of pre-intercalating ions and molecules during synthesis are rarely mentioned. Although multiple high-performance V-based host materials have been reported, the correlated optimization mechanism on enhancing the cycling stability of V-based host materials is rarely reported, which is detrimental for developing cathode materials with high cycling stability.

In this study, we successfully developed the V_2O_5 structure by pre-intercalating H^+/H_2O pillars with a facile hydrothermal reaction using commercialized V_2O_5, acetone, diluted HNO_3 as reactants, and obtained a bi-layer structured $H_{0.642}V_2O_5{\cdot}0.143H_2O$ (HVO) as a superior host material for aqueous Zn-ion batteries. This structure reconstruction dramatically enhances the cycling performance of the HVO electrode compared with that of V_2O_5. During long-term cycling, this result may be attributed to the depressed irreversible "layer-to-amorphous" phase evolution. Consequently, compared with the pristine V_2O_5, the HVO electrode has a considerably superior cycling performance with almost no capacity fading in 500 cycles at a rate current of ~0.5 A g^{-1} for aqueous Zn-ion batteries.

EXPERIMENTAL SECTION

Synthesis of HVO materials

V_2O_5 (0.5456 g) was dissolved into 70 mL of deionized water. Then, 5 mL of acetone and 2 mL of 10% nitric acid were added to the solution. After ultrasonication for 10 min, the solution was poured into a 100-mL Teflon-lined stainless-steel autoclave. The autoclave was then sealed and heated in an oven at 180°C for 24 h. The obtained green powder was filtered, washed with deionized water and ethanol, and then vacuum dried at 80°C for 12 h.

School of Advanced Materials, Peking University Shenzhen Graduate School, Shenzhen 518055, China
* Corresponding authors (emails: zhaoqh@pku.edu.cn (Zhao Q); panfeng@pkusz.edu.cn (Pan F))

Material characterization

X-ray diffraction (XRD) patterns were obtained by a high-power diffractometer (D9 Discover TXS Diffraction System) with a Cu Kα (1.5418 Å) radiation source. The morphology of these materials was evaluated by scanning electron microscopy (SEM, Carl ZEISS SUPRA 55) and transmission electron microscopy (TEM, JEM-3200FS). The composition and chemical states were evaluated by inductively coupled plasma optical emission spectrometry (ICP-OES, HORIBA Scientific JY 2000-2) and X-ray photoelectron spectroscopy (XPS, Thermo Fisher ESCALAB 250Xi). The mass change during annealing was determined through thermo-gravimetric analysis (TGA, TA instruments TGA Q500/MS Discovery) under an air atmosphere with a heating rate of 5°C min^{-1}.

Electrochemical tests

The as-prepared HVO was mixed with acetylene black and polyvinylidene fluoride with a weight ratio of 7:2:1 in *N*-methyl pyrrolidone. Then, the homogeneous slurry was pasted on a Ti foil with an average loading mass of 0.8–2 mg cm^{-1} and then dried in a vacuum oven at 110°C for 12 h. The prepared cathode was assembled in CR2032-type coin cells with a 0.8-mm-thick zinc plate anode, a glass fiber separator, and a 3 mol L^{-1} $Zn(CF_3SO_3)_2$ aqueous electrolyte under an ambient environment. Battery performance tests were performed by a NEWARE battery tester (BTS-4000) for cycling stability and rate capability in a cut-off voltage of 0.2–1.6 V. Cyclic voltammetry (CV) was performed in the potential range of 1.6–0.2 V using a CH Instrument electrochemical workstation. Electrochemical impedance spectroscopy was tested on the electrochemical workstation over the frequency range of 100 kHz–0.1 Hz. The galvanostatic intermittent titration technique (GITT) was tested by the MACCOR Model MC-16 Battery System with 10-min discharging/charging and 30-min resting.

RESULTS AND DISCUSSION

Material characterization

HVO was synthesized by a facile hydrothermal reaction using commercial V_2O_5, acetone, nitric acid, and H_2O as reactants at ~180°C. During the hydrothermal reaction, V_2O_5 is reduced by acetone, along with the breakage of V–O–V bonds and regeneration of bi-layered V–O sheets, as well as the subsequent protonation with a certain amount of H^+/H_2O intercalating into the interlayer space of HVO. This structure reconstruction has minimal effect on the morphology of the products (Fig. S1). Fig. 1a, b show the XRD patterns and the corresponding XRD refinements of V_2O_5 and HVO materials, respectively. V_2O_5 is assigned to the orthorhombic phase (ICDD No. 01-085-0601), in which the VO_5 pyramids are linked by sharing corners and edges with each other, whereas HVO shows a bi-layered structure (ICDD No. 00-025-1006), in which the pre-intercalated H^+/H_2O resides in the interlayer space. This structural reconstruction both expands the interlayer spacing and contributes to the rearrangement of VO_5 pentahedrons in HVO.

The chemical formula of HVO is confirmed using TGA in an O_2-containing atmosphere and differential scanning calorimetry (DSC) (Fig. 1c). The TGA curve can be divided into four stages, namely, the removal of the physically adsorbed H_2O (stage I, below ~132°C), the removal of crystal H_2O (stage II, between ~132 and ~243°C), the removal of H_2O from the decomposition of V–O–H bonds of HVO (stage III, between ~243 and ~334°C), and the weight gain because of the oxidation of vanadium oxide (stage IV, above ~334°C), indicating the successful pre-intercalation of proton and H_2O in HVO. Furthermore, DSC results show a considerable exothermic peak at ~675°C, which can be related to the melting of vanadium oxide.

In addition to the TGA results, the pre-intercalated H^+ and H_2O in HVO can be identified by comparing the O 1s and V 2p

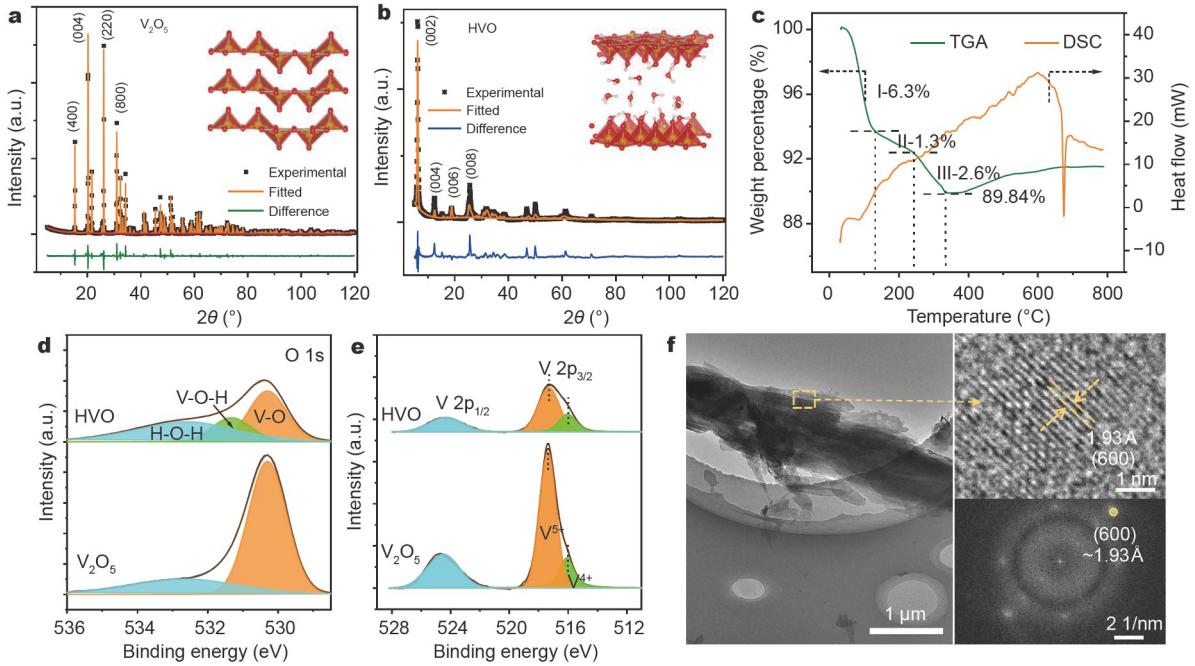

Figure 1 Material characterizations of V_2O_5 and HVO. XRD refinement of (a) V_2O_5, (b) HVO, and corresponding crystal structures (inset), (c) TGA/DSC curves of HVO product in O_2-containing atmosphere, comparison of (d) O 1s and (e) V 2p peaks of V_2O_5 and HVO, (f) HRTEM morphology and corresponding diffraction pattern of HVO.

peaks of V_2O_5 and HVO. Fig. 1d shows the characteristic peaks of H–O–H, V–O–H, and V–O bonds [37], and the intensities of V–O–H and H–O–H bonds in HVO are obviously larger than that in V_2O_5. This result indicates that the proton and H_2O are successfully intercalated into the crystal structure of HVO in the form of V–O–H bonds and structural water. Fig. 1e shows that the relatively reduced valence value of V in HVO than that in V_2O_5 is attributed to the H^+ pre-intercalation. Furthermore, the pre-intercalated H_2O and protons can be confirmed by Fourier transform infrared (FTIR) spectroscopy (Fig. S2a). The broad and intense absorption peaks at about ~3368 and ~1601 cm^{-1} correspond to H–OH bending vibrations, and the absorption peaks at ~1420 and ~981 cm^{-1} correspond to the –OH bending vibrations combining with V ions in the lattice framework. The existence of H_2O can be identified by the Raman spectra, which refer to the Raman shift value of ~1595 cm^{-1} (Fig. S2b).

High-resolution TEM (HRTEM) and correlated diffraction were applied to investigate the crystal structures of V_2O_5 and HVO. Fig. S3 provides the clear lattice fringes of (200) plane of V_2O_5 with an interlayer spacing of ~5.84 Å, and Fig. 1f shows the lattice fringes of (600) plane of HVO with an interlayer spacing of ~1.93 Å, which are consistent with that of the XRD results.

Electrode performance

The cycling performances of V_2O_5 and HVO electrodes (at 500 mA g^{-1}) in aqueous Zn-ion batteries were operated in 2032 coin-type cells with Zn plate as the anode and 3 mol L^{-1} $Zn(CF_3SO_3)_2$ as the electrolyte. Fig. 2a shows a rapid increase in the capacity delivery of the V_2O_5 electrode in the initial 55 cycles (from 75 to 451 mA h g^{-1}, highlighted in yellow). This result is primarily attributed to the electrochemical activation process. Then, the capacity decreases dramatically in subsequent cycles, showing poor cycling stability with violent fluctuations in coulombic efficiency (CE). Fig. 2b shows the correlated galvanostatic charge/discharge (GCD) profiles at the 20th, 100th, 200th, and 400th cycles, showing that the capacity delivery of V_2O_5 reduces to ~46 mA h g^{-1} at the 400th cycle, which is an ultra-low value for the capacity delivery of V-based compounds. This poor cycling performance of commercial V_2O_5 has been previously reported [38,39]. Fig. 2c shows the variation in median cell voltages (MCVs) of V_2O_5 electrodes during charge and discharge processes. The voltage polarization first reduces to a small value of ~160 mV after electrochemical activation, which is beneficial for the capacity delivery of V_2O_5. However, it rapidly increases to a very high value of ~945 mV after 200 cycles, indicating the sluggish reaction kinetics of the V_2O_5 electrode for long-term cycling.

On the basis of the above results, a basic cognition can be obtained. That is, although the structural evolution during electrochemical activation promotes the capacity delivery of the V_2O_5 electrode, the optimal structure is hard to maintain the long-term cyclic insertion/extraction of H^+/Zn^{2+} ions, which will be discussed in a later part. However, for the HVO electrode, the capacity remains nearly constant in 500 cycles, with a high capacity retention of 98.6% and a high CE of nearly 100% (Fig. 2d). Furthermore, the GCD curves at the 20th, 100th, 200th, and 400th cycles coincide very well (Fig. 2e), indicating superior cycling stability. Fig. 2f shows the constant MCVs of the HVO electrode during the charge and discharge in 500 cycles, with a well-maintained voltage polarization value of ~350 mV. Fig. S4 provides the rate performance of HVO. The structure reconstruction induced by pre-intercalating H^+ and H_2O does not contribute significant advances in the capacity and rate performances of the electrode, and its benefiting effect is primarily focused on enhancing the cycling stability of the HVO electrode.

In general, the pre-intercalated crystal water can stabilize the crystal structure of layered vanadium oxide *via* buffering the electrostatic interactions and volumetric changes during charge/

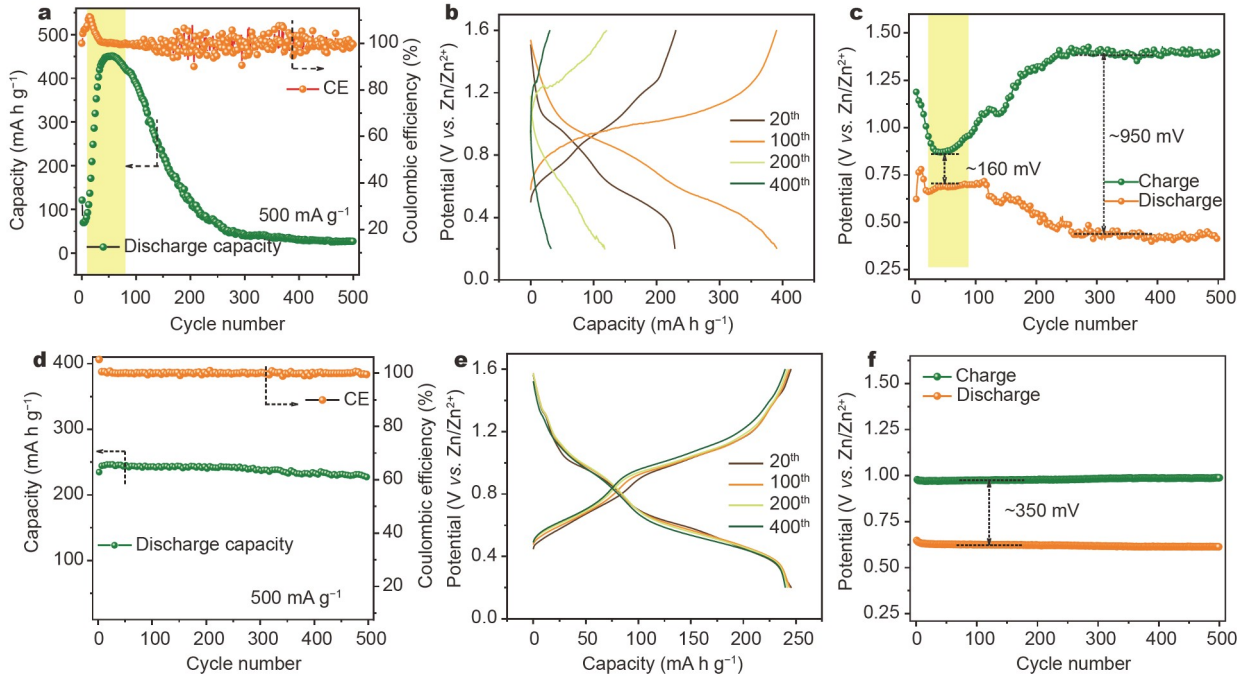

Figure 2 Comparison of the cycling performances of V_2O_5 and HVO. Cycling performances of (a) V_2O_5 and (d) HVO electrodes at a rate current of ~500 mA g^{-1}. Comparison of charge/discharge profiles at the 20th, 100th, 200th, and 400th cycles of (b) V_2O_5 and (e) HVO electrodes. The corresponding MCV variations during the charge/discharge processes of (c) V_2O_5 and (f) HVO electrodes.

discharge cycles [35]. However, the effect of H^+ intercalation is rarely reported. The interlayer water in HVO is removed *via* simply annealing at ~250°C for 2 h to obtain deep insights into the effect of pre-intercalated H^+ on the electrode performance. The obtained product is denoted as HVO-250. Fig. S5 shows the cycling performance of the HVO-250 electrode, which shows no capacity fading in 300 cycles at a rate current of ~500 mA g^{-1} and high capacity retention of ~96% in 1200 cycles at a rate current of ~2000 mA g^{-1}, indicating superior cycling stability. Moreover, the enhanced rate performance of the HVO-250 electrode is provided (Fig. S6). The results indicate that HVO-250 shows slightly better capacity, rate, and cycling performances than HVO. That is, a single H^+ pre-intercalation can stabilize the cycling stability of V-based host materials.

Depressed "layer-to-amorphous" phase evolution in the HVO electrode

In general, the structural factors dominate the cycling stability of host materials in aqueous batteries [40]. To clarify the stabilizing mechanism, we compared the XRD patterns of V_2O_5 and HVO at fully charged and discharged states of the 1st and 5th cycles (Fig. S7). The pristine HVO electrode presents a reduced interlayer spacing (~11.68 Å, 2θ = 7.38°) because of the drying process in a vacuum oven at ~110°C, and the structures of V_2O_5 and HVO are well maintained in the first five cycles. Fig. 3 shows the XRD and TEM comparisons of the V_2O_5 and HVO electrodes during long-term cycles (the 50th, 150th, and 300th cycles at a rate current of 500 mA g^{-1}). Fig. 3a shows the "layer-to-amorphous" phase transition evolution of V_2O_5, in which the V_2O_5 nanocrystal is obtained at the 50th cycle, with weak characteristic peaks of the (204), (800), (024), and (620) planes of V_2O_5. Moreover, it converts to a completely amorphous state with no characteristic peaks of V_2O_5 at the 150th and 300th cycles.

Fig. 3b, c display the HRTEM morphology and corresponding diffraction pattern of V_2O_5 after the 50th cycle, respectively. Its features are similar to those of the amorphous phase with a clear diffraction ring, i.e., in the nanocrystalline feature with multiple nano-domains (Fig. S8). Considering the electrode performance,

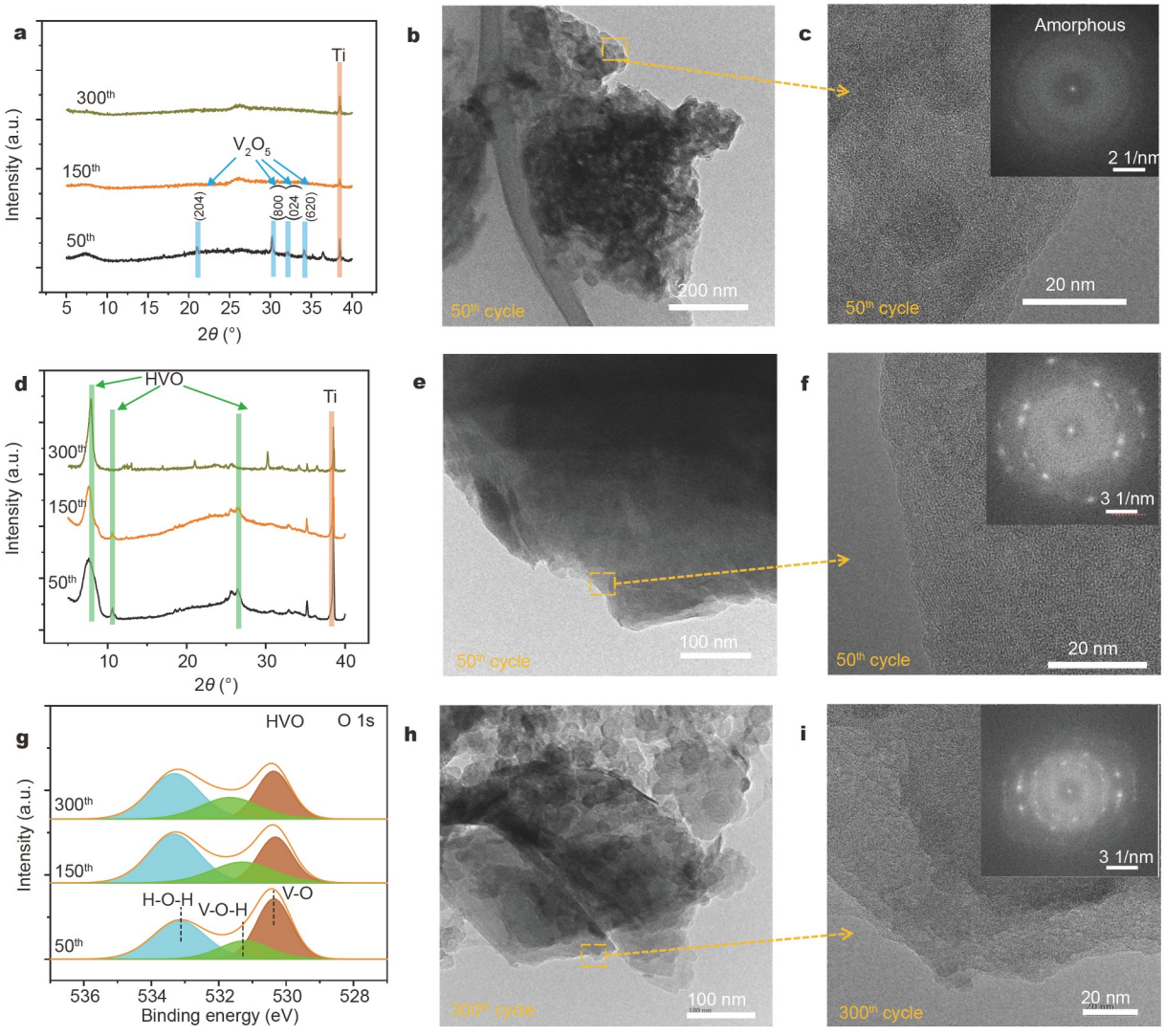

Figure 3 Depressed "layer-to-amorphous" phase transition for the superior cycling performance of HVO. XRD patterns of (a) V_2O_5 and (d) HVO electrodes at the 50th, 150th, and 300th cycles at 500 mA g^{-1}. (b, c) HRTEM morphologies and diffraction pattern of the V_2O_5 electrode at the 50th cycle. (g) XPS analysis of O 1s peaks of HVO electrode at various cycles. HRTEM morphologies and diffraction patterns of HVO electrodes at the (e, f) 50th and (h, i) 300th cycles. Note: all the electrodes are at charged state.

we conclude that V_2O_5 in nanocrystal state, which is derived from the electrochemical activation in the first 50 cycles, can enhance the charge storage of carrier ions (i.e., H^+/Zn^{2+}), whereas V_2O_5 in a completely amorphous state is detrimental for the capacity delivery of the electrode. Thus, the enhanced capacity of V_2O_5 in the first 55 cycles (Fig. 2a) is primarily attributed to the generation of V_2O_5 nanocrystals, whereas the subsequent rapid capacity fading can be attributed to the formation of amorphous V_2O_5. The occurrence of amorphous phases represents a structure collapse of V_2O_5 against the cyclic H^+/Zn^{2+} insertion/extraction process, which blocks the transport channels for H^+/Zn^{2+}, and results in a rapid capacity fading.

Fig. 3d shows the structure evolution of HVO during cycling, in which the bi-layered structure of HVO can be well maintained in 300 cycles. Fig. 3e, f provide the HRTEM morphology and corresponding diffraction pattern of HVO at the 50th cycle. The diffraction spots feature a polycrystalline phase, which is well maintained even after 300 cycles, as shown in Fig. 3h, i. These results indicate that structure reconstruction in HVO can stabilize the crystal structure against the cyclic H^+/Zn^{2+} insertion/extraction process, which enables high cycling stability. The pre-intercalated H^+ and H_2O play an important role in stabilizing the bi-layered structure of HVO, which remains unchanged during the structure evolution of long-term cycling, as shown in Fig. 3g. However, the intensity of H^+/H_2O in the V_2O_5 electrode greatly changes (Fig. S9) because of the serious structure collapse in the "layer-to-amorphous" phase evolution. Thus, H^+/H_2O pre-intercalations act as stabilizing pillars to inhibit the "layer-to-amorphous" phase transition in the HVO electrode, which is responsible for the enhanced cycling stability.

Synthetic proton and Zn^{2+} intercalation mechanism

Because HVO is a promising host candidate for aqueous Zn-ion batteries, we focus on its reaction mechanism. Fig. 4a, b show the charge/discharge curves and corresponding XRD patterns of the HVO electrode at different states. We observe a reversible contraction/expansion of (002) plane during the discharge/recharge process, and some by-products (2θ = 6.6°) appear/diminish at the discharged/charged states. The corresponding electrode morphologies are provided in Fig. 4c, d, which show the reversible disappearance and generation of the by-products upon cycling. SEM morphology and corresponding energy dis-

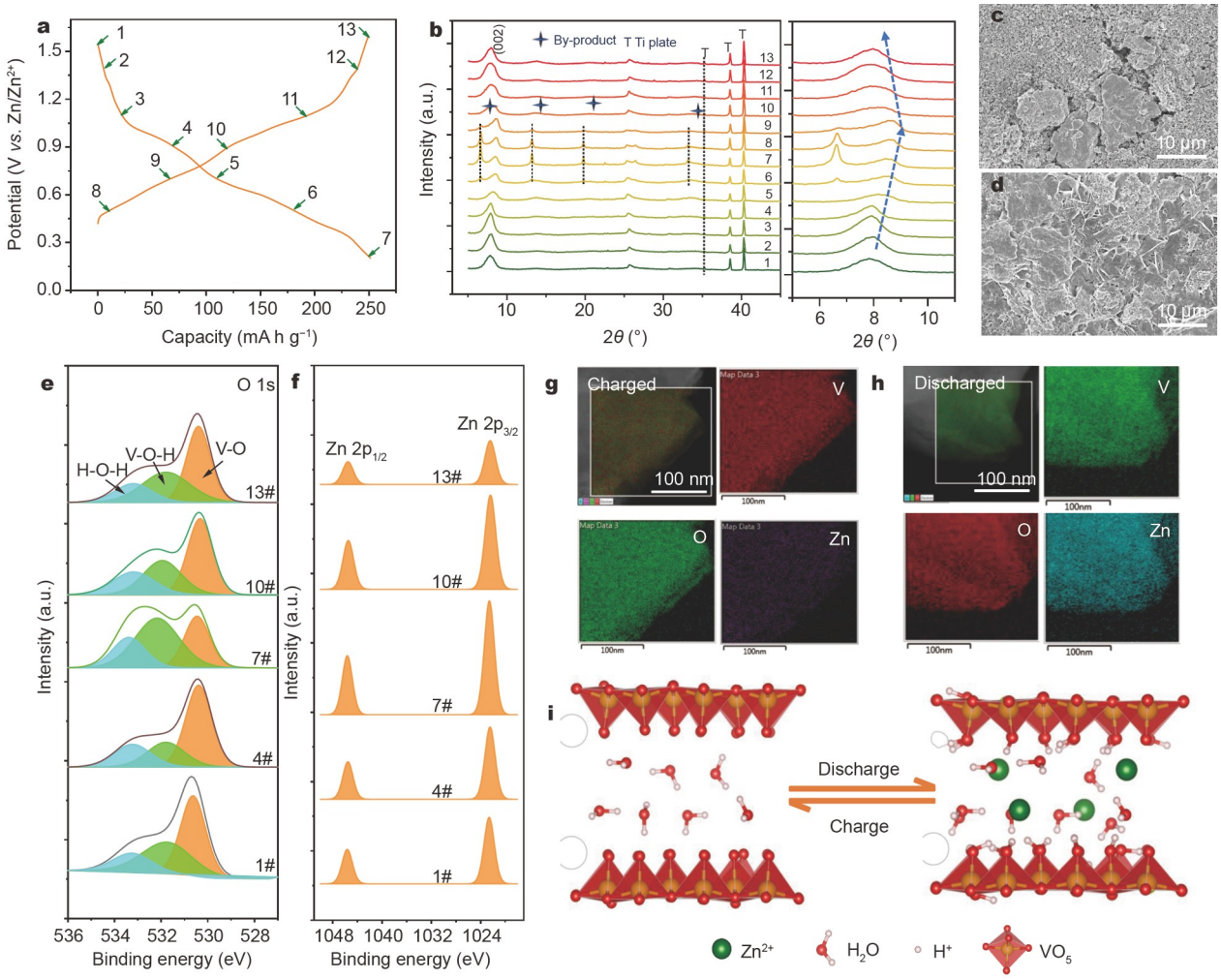

Figure 4 Charge storage mechanism of the HVO electrode. (a) Charge/discharge curves of the HVO electrode at a rate current of 0.1 A g^{-1}, and (b) corresponding XRD patterns at different states. SEM morphologies of the HVO electrode at (c) charged and (d) discharged states. Analysis of XPS peaks of (e) O 1s and (f) Zn 2p at different states. TEM-EDS mapping results of HVO at the (g) charged and (h) discharged states. (i) Schematic of the synthetic H^+/Zn^{2+} intercalation mechanism of the HVO electrode.

persive X-ray spectroscopy (EDS) analysis results (Fig. S10) indicate that the by-product is composed of Zn, O, F, and S elements. Combining XRD, SEM, and EDS results, we consider that the by-product belongs to the zinc hydroxide trifluoromethane-sulfonic hydrate ($Zn_x(OH)_y(CF_3SO_3)_{2x-y}\cdot nH_2O$), which is solid evidence for the proton intercalation upon discharge [41]. The H^+ intercalation can be confirmed by the XPS analysis of O 1s peaks in Fig. 4e. The intensity of V–O–H bonds enhances upon discharge and reduces upon recharge processes, showing a reversible intercalation/extraction of protons in the HVO electrode.

We confirm the reversible Zn^{2+} intercalation/extraction in HVO is from the following two aspects. First, XPS results indicate that the intensity of Zn 2p peaks enhances upon discharge and reduces upon charge, corresponding to the intercalation/extraction processes of Zn^{2+} in HVO (Fig. 4f). Second, TEM-EDS mapping results show an obvious Zn enrichment in the discharged HVO electrode, whereas, for the charged electrode, the presence of Zn enrichment is relatively rare (Fig. 4g, h). Thus, a synthetic proton and Zn^{2+} intercalation mechanism is proposed in this work (Fig. 4i), which is accompanied by the reversible contraction/expansion of interlayer spacing of the HVO electrode. Concerning the discharging capacity of the 2nd cycle of HVO and using ICP spectrometry, we calculate the reaction equation of the HVO electrode during the discharging/charging process as follows:

$$H_{0.10}Zn_{0.27}V_2O_5\cdot xH_2O+1.59H^++0.13Zn^{2+}+yH_2O+1.85e^- \leftrightarrow H_{1.69}Zn_{0.40}V_2O_5\cdot(x+y)H_2O. \quad (1)$$

As demonstrated in Equation (1), the proton and Zn^{2+} insertions contribute ~85.9% and ~14.1% of the capacity delivery, respectively. Proton insertion dominates the capacity delivery of HVO. The proton displays a smaller ion radius and charge density compared with Zn^{2+}. HVO exhibits excellent diffusion kinetics, benefiting the rate performance of HVO in Fig. S4. We conducted the CV curves of HVO at different scanning rates (Fig. S11). The results indicate that all the calculated *b* values of oxidative/reductive peaks are close to 1, demonstrating the dominating role of pseudo-capacitive diffusion in capacity delivery. The contribution of pseudo-capacitive diffusion on capacity delivery is as high as 92.4%, illustrating the dominant role of pseudo-capacitive diffusions. Furthermore, the corresponding average diffusion coefficients, calculated by GITT (Fig. S12), are shown as ~2.14×10^{-10} and ~2.99×10^{-10} $cm^2\,s^{-1}$ for the discharge and charge processes of the HVO electrode, respectively, which is among the highest diffusion kinetics of V-based cathode materials (Table S1).

CONCLUSION

We successfully synthesized an H^+ and H_2O pre-intercalated HVO through a facile hydrothermal reaction. Compared with pristine V_2O_5, HVO presents considerably higher cycling stability mainly because of its tough structure optimized by H^+ and H_2O pre-intercalations. The bi-layered structure of HVO can maintain well even after 300 cycles at 500 mA g^{-1}. Moreover, we reveal the proton and Zn^{2+} co-intercalation reaction mechanism of HVO for aqueous Zn-ion batteries in which proton insertion dominates the electrode reaction and enables high reaction kinetics. This work presents a new viewpoint for designing next-generation high-performance cathode materials for aqueous batteries.

Received 11 April 2021; accepted 4 June 2021; published online 30 July 2021

1 Tian Y, Liu X, Xu L, *et al.* Engineering crystallinity and oxygen vacancies of Co(II) oxide nanosheets for high performance and robust rechargeable Zn-air batteries. Adv Funct Mater, 2021, 31: 2101239
2 Wu X, Xu Y, Zhang C, *et al.* Reverse dual-ion battery *via* a $ZnCl_2$ water-in-salt electrolyte. J Am Chem Soc, 2019, 141: 6338–6344
3 Jia H, Wang Z, Tawiah B, *et al.* Recent advances in zinc anodes for high-performance aqueous Zn-ion batteries. Nano Energy, 2020, 70: 104523
4 Qin R, Wang Y, Zhao Q, et al. EQCM for in-depth study of metal anodes for electrochemical energy storage. Chinese J Struct Chem, 2020, 39: 605–614
5 Liu M, Zhao Q, Liu H, *et al.* Tuning phase evolution of β-MnO_2 during microwave hydrothermal synthesis for high-performance aqueous Zn ion battery. Nano Energy, 2019, 64: 103942
6 Zhao Q, Ding S, Song A, et al. Tuning structure of manganese oxides to achieve high-performance aqueous Zn batteries. Chinese J Struct Chem, 2020, 39: 388–394
7 Zhao Q, Chen X, Wang Z, *et al.* Unravelling H^+/Zn^{2+} synergistic intercalation in a novel phase of manganese oxide for high-performance aqueous rechargeable battery. Small, 2019, 15: 1904545
8 Sa N, Kinnibrugh TL, Wang H, *et al.* Structural evolution of reversible Mg insertion into a bilayer structure of $V_2O_5\cdot nH_2O$ xerogel material. Chem Mater, 2016, 28: 2962–2969
9 McColl K, Corà F. Phase stability of intercalated V_2O_5 battery cathodes elucidated through the Goldschmidt tolerance factor. Phys Chem Chem Phys, 2019, 21: 7732–7744
10 Zhang B, Li Z, Li Q, et al. Insights into the H_2O/V_2O_5 interface structure for optimizing water-splitting. Chinese J Struct Chem, 2020, 39: 189–199
11 Yi H, Qin R, Ding S, *et al.* Structure and properties of Prussian blue analogues in energy storage and conversion applications. Adv Funct Mater, 2020, 31: 2006970
12 Ma L, Chen S, Long C, *et al.* Achieving high-voltage and high-capacity aqueous rechargeable zinc ion battery by incorporating two-species redox reaction. Adv Energy Mater, 2019, 9: 1902446
13 Qin R, Wang Y, Zhang M, *et al.* Tuning Zn^{2+} coordination environment to suppress dendrite formation for high-performance Zn-ion batteries. Nano Energy, 2021, 80: 105478
14 Zheng J, Tan G, Shan P, *et al.* Understanding thermodynamic and kinetic contributions in expanding the stability window of aqueous electrolytes. Chem, 2018, 4: 2872–2882
15 Wang Z, Hu J, Han L, *et al.* A MOF-based single-ion Zn^{2+} solid electrolyte leading to dendrite-free rechargeable Zn batteries. Nano Energy, 2019, 56: 92–99
16 Cui Y, Zhao Q, Wu X, *et al.* An interface-bridged organic-inorganic layer that suppresses dendrite formation and side reactions for ultra-long-life aqueous zinc metal anodes. Angew Chem Int Ed, 2020, 59: 16594–16601
17 Kang Z, Wu C, Dong L, *et al.* 3D porous copper skeleton supported zinc anode toward high capacity and long cycle life zinc ion batteries. ACS Sustain Chem Eng, 2019, 7: 3364–3371
18 Ko JS, Geltmacher AB, Hopkins BJ, *et al.* Robust 3D Zn sponges enable high-power, energy-dense alkaline batteries. ACS Appl Energy Mater, 2019, 2: 212–216
19 Zhao Q, Song A, Zhao W, *et al.* Boosting the energy density of aqueous batteries *via* facile Grotthuss proton transport. Angew Chem, 2020, 133: 4215–4220
20 Huang J, Tang X, Liu K, *et al.* Interfacial chemical binding and improved kinetics assisting stable aqueous Zn-MnO_2 batteries. Mater Today Energy, 2020, 17: 100475
21 Xu D, Wang H, Li F, *et al.* Conformal conducting polymer shells on V_2O_5 nanosheet arrays as a high-rate and stable zinc-ion battery cathode. Adv Mater Interfaces, 2019, 6: 1801506

22 Li W, Han C, Wang Y, *et al.* Structural modulation of manganese oxides for zinc-ion batteries. Chinese J Struct Chem, 2020, 39: 31–35
23 Zhao Q, Song A, Ding S, *et al.* Preintercalation strategy in manganese oxides for electrochemical energy storage: Review and prospects. Adv Mater, 2020, 32: 2002450
24 Tan Q, Li X, Zhang B, *et al.* Valence engineering *via in situ* carbon reduction on octahedron sites Mn_3O_4 for ultra-long cycle life aqueous Zn-ion battery. Adv Energy Mater, 2020, 10: 2001050
25 Yang W, Dong L, Yang W, *et al.* 3D oxygen-defective potassium vanadate/carbon nanoribbon networks as high-performance cathodes for aqueous zinc-ion batteries. Small Methods, 2020, 4: 1900670
26 Yao X, Zhao Y, Castro FA, *et al.* Rational design of preintercalated electrodes for rechargeable batteries. ACS Energy Lett, 2019, 4: 771–778
27 Yang Y, Tang Y, Fang G, *et al.* Li^+ intercalated $V_2O_5{\cdot}nH_2O$ with enlarged layer spacing and fast ion diffusion as an aqueous zinc-ion battery cathode. Energy Environ Sci, 2018, 11: 3157–3162
28 He P, Zhang G, Liao X, *et al.* Sodium ion stabilized vanadium oxide nanowire cathode for high-performance zinc-ion batteries. Adv Energy Mater, 2018, 8: 1702463
29 Tang B, Fang G, Zhou J, *et al.* Potassium vanadates with stable structure and fast ion diffusion channel as cathode for rechargeable aqueous zinc-ion batteries. Nano Energy, 2018, 51: 579–587
30 Ming F, Liang H, Lei Y, *et al.* Layered $Mg_xV_2O_5{\cdot}nH_2O$ as cathode material for high-performance aqueous zinc ion batteries. ACS Energy Lett, 2018, 3: 2602–2609
31 Patridge C. Probing local electronic and geometric changes of hydrated calcium vanadium oxide ($Ca_xV_2O_5{\cdot}yH_2O$) upon Zn ion intercalation. J Coord Chem, 2019, 72: 1253–1266
32 Wang X, Xi B, Ma X, *et al.* Boosting zinc-ion storage capability by effectively suppressing vanadium dissolution based on robust layered barium vanadate. Nano Lett, 2020, 20: 2899–2906
33 Liu Y, Pan Z, Tian D, *et al.* Employing "one for two" strategy to design polyaniline-intercalated hydrated vanadium oxide with expanded interlayer spacing for high-performance aqueous zinc-ion batteries. Chem Eng J, 2020, 399: 125842
34 Bin D, Huo W, Yuan Y, *et al.* Organic-inorganic-induced polymer intercalation into layered composites for aqueous zinc-ion battery. Chem, 2020, 6: 968–984
35 Yan M, He P, Chen Y, *et al.* Water-lubricated intercalation in $V_2O_5{\cdot}nH_2O$ for high-capacity and high-rate aqueous rechargeable zinc batteries. Adv Mater, 2018, 30: 1703725
36 Zhao J, Ren H, Liang Q, *et al.* High-performance flexible quasi-solid-state zinc-ion batteries with layer-expanded vanadium oxide cathode and zinc/stainless steel mesh composite anode. Nano Energy, 2019, 62: 94–102
37 Pang Q, Sun C, Yu Y, *et al.* $H_2V_3O_8$ nanowire/graphene electrodes for aqueous rechargeable zinc ion batteries with high rate capability and large capacity. Adv Energy Mater, 2018, 8: 1800144
38 Hu P, Yan M, Zhu T, *et al.* Zn/V_2O_5 aqueous hybrid-ion battery with high voltage platform and long cycle life. ACS Appl Mater Interfaces, 2017, 9: 42717–42722
39 Liu W, Dong L, Jiang B, *et al.* Layered vanadium oxides with proton and zinc ion insertion for zinc ion batteries. Electrochim Acta, 2019, 320: 134565
40 Zheng Z, Weng M, Yang L, *et al.* Thermodynamically revealing the essence of order and disorder structures in layered cathode materials. Chinese J Struct Chem, 2019, 38: 2020–2026
41 Oberholzer P, Tervoort E, Bouzid A, *et al.* Oxide *versus* nonoxide cathode materials for aqueous Zn batteries: An insight into the charge storage mechanism and consequences thereof. ACS Appl Mater Interfaces, 2019, 11: 674–682

Acknowledgements This work was supported by the Basic and Applied Basic Research Foundation of Guangdong Province (2019A1515110094).

Author contributions Wang Y performed the sample preparation and electrochemical tests. Chen C, Ren H, Qin R, Yi H, and Ding S analyzed the charge storage mechanism. Zhao Q wrote the paper with support from Li S. All authors contributed to the general discussion.

Conflict of interest The authors declare that they have no conflict of interest.

Supplementary information Supporting data are available in the online version of the paper.

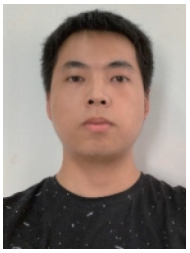

Yuetao Wang received his BE degree from the College of Chemistry and Molecular Engineering at Peking University (PKU, China) in 2018. He is currently completing his PhD degree under the supervision of Prof. Feng Pan at the School of Advanced Materials, Peking University Shenzhen Graduate School, China. His research interests focus on aqueous zinc-ion batteries, especially on vanadium-based cathode materials.

Qinghe Zhao received his BS degree from the University of Science and Technology of Beijing (USTB, China) in 2010 and earned his PhD degree from the School of Advanced Materials at USTB in 2016, majoring in the electrochemical corrosion behavior of Fe-based alloys, under the supervision of Prof. Minxu Lu. Dr. Zhao is now an associate researcher at the School of Advanced Materials, Peking University Shenzhen Graduate School, China. His research interests primarily focus on the key materials and technologies for energy storage and conversion applications, including electrocatalysts, zinc-ion batteries, and sodium-ion batteries.

Feng Pan, chair-professor, founding dean of the School of Advanced Materials, Peking University Shenzhen Graduate School, director of the National Center of Electric Vehicle Power Battery and Materials for International Research, received his BS degree from the Department of Chemistry, PKU in 1985 and PhD degree from the Department of Pure & Applied Chemistry, University of Strathclyde, UK with "Patrick D. Ritchie Prize" for the best PhD in 1994. Prof. Pan has been engaged in the fundamental research of structure chemistry, exploring "Material Gene" for Li-ion batteries and developing novel energy conversion-storage materials and devices. He also received the 2018 ECS Battery Division Technology Award.

水系可充锌电池中$H_{0.642}V_2O_5{\cdot}0.143H_2O$正极的高循环稳定性机制研究

王乐涛, 陈传玺, 任恒宇, 秦润之, 易浩聪, 丁收香, 李洋, 姚路, 李舜宁, 赵庆贺*, 潘锋*

摘要 水系可充电池中过渡金属氧化物宿主材料的循环稳定性是影响其长时间服役性能的关键. 本文通过简单的预嵌入方法, 将一定量的质子和水分子预嵌入到V_2O_5晶格中, 重构了晶体结构, 获得了高性能水系锌电池中的$H_{0.642}V_2O_5{\cdot}0.143H_2O$(HVO)层状正极材料. 得益于该结构重构, 钒氧化物正极循环过程中的"层状/非晶"结构演化过程被抑制, 由此获得极高循环稳定性(在0.5 A g^{-1}电流密度下循环500圈几乎无衰减). 此外, 该研究报道了HVO正极中质子和锌离子协同嵌入的储能机制, 为下一代高性能钒基正极材料的设计提供了一种新的理念.

